Silica hollow bottle resonators for use as whispering gallery mode based chemical sensors

2015 J. Opt. 17 125011

(http://iopscience.iop.org/2040-8986/17/12/125011)

IOP Publishing Journal of Optics
J. Opt. 17 (2015) 125011 (7pp) doi:10.1088/2040-8978/17/12/125011

Silica hollow bottle resonators for use as whispering gallery mode based chemical sensors

Razvan-Ionut Stoian[1], **Khoa V Bui and A T Rosenberger**

Department of Physics, Oklahoma State University, Stillwater, OK 74078-3072, USA

E-mail: atr@okstate.edu

Received 19 May 2015, revised 10 September 2015
Accepted for publication 29 September 2015
Published 5 November 2015

Abstract

A simple three-step method for making silica hollow bottle resonators (HBRs) was developed. This procedure is advantageous because it uses commercially available materials, is cost effective, and is easy to implement. Additionally, the use of these HBRs as whispering gallery mode based chemical sensors is demonstrated by preliminary absorption sensing results in the near infrared (1580–1660 nm) using a trace gas (CH_4) in air at atmospheric pressure and a dye (SDA2072) in methanol solution.

Keywords: silica resonator fabrication, whispering-gallery modes, hollow microresonators, chemical sensors

1. Introduction

Gas and liquid sensing in the near infrared (NIR) is extremely important for the analysis of various chemical species in industrial settings and in the life sciences. Some sensing technologies in the NIR make use of passive optical resonators probed over a range of tens of GHz using a frequency-scanned tunable laser. In particular, silica-based whispering gallery mode (WGM) resonators such as microspheres have been widely used in chemical sensing for more than a decade. The work presented herein develops another type of silica WGM chemical sensor.

Here we describe a method for the fabrication of a hollow bottle resonator (HBR) that is not only simpler than some earlier schemes but also partially automated; in addition, we give some preliminary examples of its use in chemical absorption sensing via a technique that is new for hollow resonators. The HBR is made by etching a silica capillary to reduce its wall thickness, then heating while pressurizing to form a bulge that will provide axial confinement of its WGMs, which are excited via tapered-fiber coupling. The HBR is thus a hybrid of the capillary-based optical ring resonator [1–6] and the bottle microresonator [7–12]. The result is sometimes called an HBR [13–19] and sometimes a 'bubble' microresonator [17–31], roughly depending on whether the bulge diameter is slightly or significantly greater than the original diameter of the capillary.

As a sensor, the HBR takes advantage of intracavity enhancement (because it is a microresonator), and in addition it combines the advantages of capillary-based optical ring resonators (because it is hollow) and whispering-gallery bottle resonators (because of the bottle shape). Capillary-based optical ring resonators [1–6] are advantageous because they permit internal sensing, which means that much smaller volumes of analyte are required, and it is easy to incorporate the sensor into microfluidic and/or chromatographic systems. Bottle resonators [7–12] provide the benefits of high quality factor (Q), tunability (by stretching), axial mode confinement, and mode selectivity (e.g., by positioning the coupling fiber). The HBR [13–31], then, has all of these positive attributes, and can be used in any application where a capillary-based sensor could, while providing significantly enhanced sensitivity owing to the HBR's one- to two-order-of-magnitude higher Q. The internal sensitivities found here are several times better than the external sensitivities demonstrated earlier with solid microresonators [32–35].

[1] *Present address:* Department of Electrical and Computer Engineering, Box 90291, Duke University, Durham, NC 27708, USA.

2. HBR Fabrication

The method that gave the best results in terms of obtaining a small wall thickness (<10 μm) in a silica HBR of high optical quality is an original variation on the pioneering work of Murugan *et al* [14] and Henze *et al* [24]. Unlike previous approaches, our method is simple and cost effective in that it does not use a CO_2 laser [15, 20, 22–25, 29] or arc discharge [14, 16, 18, 19, 31] with in-house produced capillaries, but rather commercial silica capillaries and a H_2/O_2 jeweler's torch. The fabrication procedure follows this sequence: after HF etching to reduce the wall thickness, and removal of the capillary's polyimide coating by hot sulfuric acid, the uncoated middle section of the capillary is uniformly heated using a hydrogen–oxygen torch and compressed air is introduced into the sealed capillary channel. The softened region of the capillary then expands, forming a bulge whose size and shape is determined by the compressed air pressure, flame size, and flame temperature.

2.1. Step 1—Etching

The commercial silica capillaries used for making HBRs were produced by Polymicro Technologies™. Two types of polyimide-coated capillaries were chosen for their relatively thin walls: TSP700850™ (802 μm silica outer diameter, 51 μm silica wall thickness, 24 μm polyimide coating thickness) and TSP250350™ (324 μm silica outer diameter, 37 μm silica wall thickness, 18 μm polyimide coating thickness). The small silica wall thickness reduces the required etching time.

Aqueous HF was used for etching, since the handling of HF vapors, which is a procedure specific to dry etching [36], requires expensive safeguards and sophisticated hardware. The etching solution that was used consisted of equal volumes of aqueous HF (48%—Sigma Aldrich) and methanol. The HF–methanol solution allowed for uniform and consistent etching. Preliminary results showed that etching with aqueous HF alone had two important drawbacks: a high etching rate that is not easily adjustable, and a highly irregular etched surface. Adding methanol greatly improves the outcome in that the etched inner surface is smooth well into the sub-μm range, and the etching rate is decreased and more easily controlled.

A schematic of the etching apparatus is shown in figure 1. One or two capillaries (7 cm to 20 cm in length) are epoxied into holes pierced near the bottoms of two plastic cuvettes. Initially, 1 mL of HF/methanol solution is pipetted into each cuvette (stage 1 of figure 1) and the cuvettes are sealed using paraffinated paper and plastic caps. Etching is performed by replenishing the HF solution inside the capillaries every 10 min, following the 20 s sequence shown in figure 1. First, the HF mixture in one of the cuvettes is pushed by compressed air through the capillaries (a syringe pump feed is connected through an opening near the top of the first cuvette) to produce the situation shown in stage 2. Then, after allowing a few seconds for the solution to settle, the entire volume in the second cuvette (2 mL) is run through the capillaries into the first cuvette (stage 3), and after the solution settles, 1 mL of the solution is returned to the second cuvette so that at the end of the process (stage 4), the two plastic containers contain equal volumes of HF solution. The total etching time ranges from 4 to 6 h depending on the initial and final wall thicknesses.

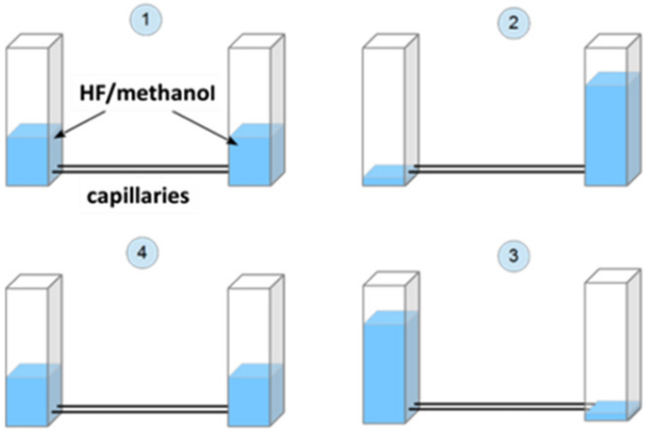

Figure 1. The sequence of events for HF circulation through the capillaries. A single 20 s pumping cycle is repeated every 10 min, following the sequence indicated in stages 1–4.

Although etching is the lengthiest part of the fabrication process, this step is automated so as to require a minimal time commitment from the operator. The task of HF circulation through the capillaries is performed using a computer controlled 60 cm^3 syringe pump. The basis of this pump is a linear stage driven by a bipolar stepper motor with USB-based controller (Phidgets Inc.) operated by a LabVIEW program. The 20 s duration of the sequence was chosen to ensure a consistent average etching rate. The speed at which HF is pushed back and forth in the capillaries strongly affects this rate.

The average etching rate ranged from 115 to 125 nm min^{-1}; the lower value was typical for the larger-diameter capillaries and the higher value was typical for the smaller capillaries. Some variation in final wall thickness is due to the fact that the initial wall thicknesses of the capillaries can vary over a range of 11 μm for TSP700850 and 6 μm for TSP250350. The final wall thickness, after creating the bulge in Step 3, was estimated to be between 5 and 10 μm. This estimate was made by using a simple optical microscope with ~5 μm resolution to observe the ends of etched capillaries and occasionally the cross section of a broken HBR. Variations in the initial wall thickness and in the etching process produced only a small dispersion in the desired final wall thickness.

The good consistency of the etching rate would not be possible without etching taking place in a very small volume. Etching starts strongly as soon as fresh HF mixture is introduced into the capillary. However, due to the small reaction volume, the etching agent quickly becomes saturated with dissolved silica crystals. This *self-quenching* process is extremely important because it ensures that toward the end of each 10 min etching cycle, the internal surface of the capillary

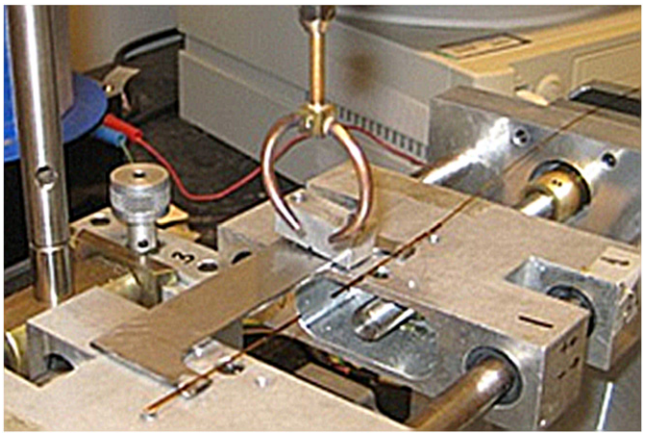

Figure 2. The positioning of the jeweler's torch relative to the support holding the etched capillary.

becomes smoother; this smoothness improves further as the HF mixture loses its efficiency late in the etching process.

2.2. Step 2—Coating removal

In order to create the HBR, the region in the middle of the length of the etched capillary must undergo chemical treatment in a hot (270 °C) H_2SO_4 bath for 15–20 min, so that a small section (1.5 cm) of the 18–24 μm thick polyimide coating can be removed. Immediately after the coating comes off, methanol must be applied to the uncoated region in a few vigorous short bursts. An additional short (5 min) hot acid treatment using clean H_2SO_4 can be further applied to the bare capillary in case the initial treatment does not fully detach microscopic portions of the coating. Care must be taken that the detached coating not disintegrate in the H_2SO_4 bath and render the solution cloudy-brown, thereby irreversibly downgrading the optical quality of the uncoated capillary.

2.3. Step 3—Heating and pressurization

After coating removal, the etched capillary is epoxied to the two tines of a U-shaped metal holder (see figure 2) for convenient handling. One end of the etched capillary is sealed using a small drop of epoxy, and the other end is connected to a syringe feed for pressurization. The ensemble is then mounted on the same rig that contains the hydrogen–oxygen jeweler's torch. The nozzle on the torch must have a shape that will ensure uniform flame coverage around the silica capillary. A modified crescent-shaped nozzle as shown in figure 2, sonicated in a methanol bath for 10 min before every usage, produced excellent results.

The syringe is operated manually, increasing the internal air pressure by 150–800 Torr. As soon as a bulge of desired size was formed the flame was quickly withdrawn and the newly formed bottle resonator was left to cool down. For a given final pressure, flame temperature (dictated by the oxygen content), and capillary wall thickness, it was possible to obtain silica HBRs of various lengths, wall thicknesses at the point of maximum bulge diameter, and shapes (bottle or bubble). Figure 3 shows a typical HBR obtained through this method. The HBR is larger than typical solid bottle resonators [7–12]; multiple identical HBRs are not necessary; and the utility of the HBR does not depend on the precision of its dimensions. For these reasons, no attempt was made to achieve some arbitrary level of accuracy in the fabrication process.

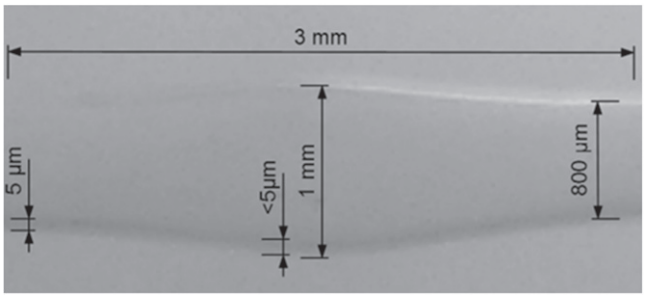

Figure 3. A hollow bottle resonator obtained by manual compression of air inside the capillary.

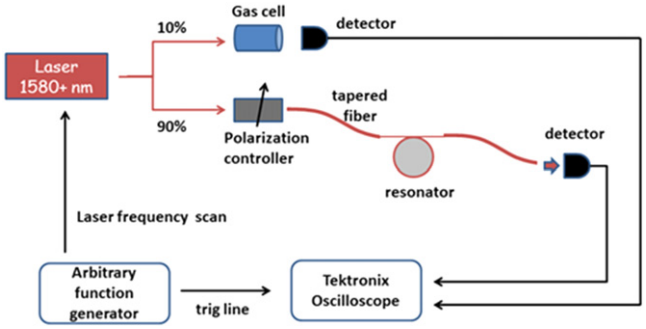

Figure 4. Simplified schematic of a generic HBR chemical sensing experiment. The gas cell may be used as a reference for trace gas detection.

3. Preliminary sensing results

3.1. Methodology

Chemical sensing with the silica HBR is performed in a manner similar to that used for chemical sensing using a silica microsphere. As illustrated in figure 4, tunable and polarization-controlled laser light is injected into an optical fiber whose tapered region permits excitation of the HBR's WGMs of either polarization family (TE or TM).

As the laser frequency scans through a WGM resonance, the throughput shows a dip of Lorentzian profile whose width is proportional to the total loss, intrinsic loss (predominantly surface scattering) plus coupling loss. Interaction of the analyte with the evanescent component of a WGM results in a change in the detected throughput signal. Because of the HBR's thin wall, some WGMs have internal evanescent fields, allowing either external or internal sensing, as shown in figure 5. The more advantageous internal sensing was used for the results presented in the next subsection.

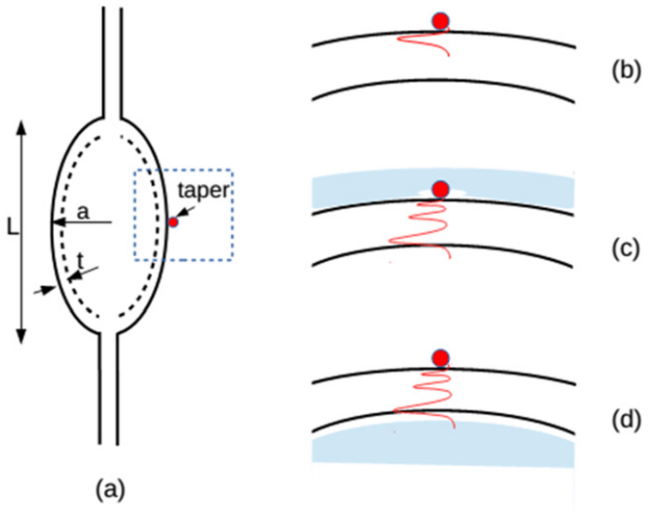

Figure 5. Sensing principle for external and internal WGM-based sensing. (a) Schematic of HBR with length L, equatorial radius a, and wall thickness t. The region in the dashed box is rotated and expanded in the following parts of the figure. (b) Fundamental radial mode with external evanescent fraction only. (c) External and (d) internal evanescent sensing, using a higher-radial-order mode having both external and internal evanescent fractions to interact with external and internal analytes, respectively.

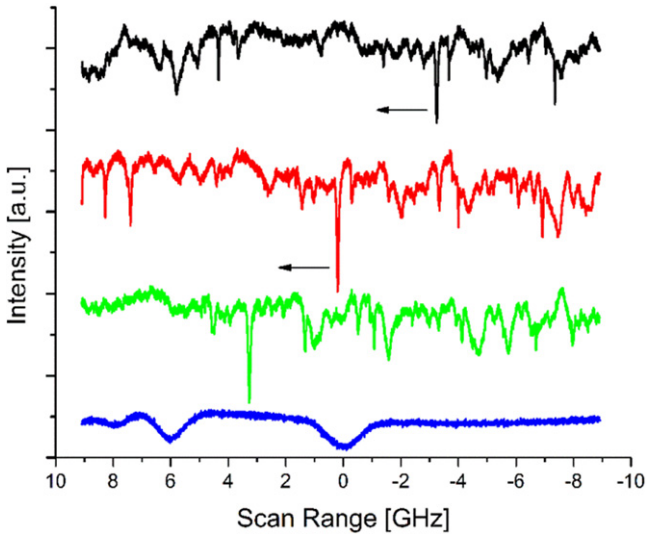

Figure 6. WGM affected by CH_4 absorption lines around 1641.1 nm in a 1% CH_4/air mixture. The bottom blue trace shows the absorption features as observed in the reference cell transmission for pure CH_4 at 100 Torr. The arrow indicates the frequency shift of the affected WGM as it is moved into and out of the main absorption resonance: top trace, WGM frequency below resonance; second trace from top, on resonance; third trace from top, WGM frequency above resonance.

Several microresonator-based sensing methods have commonly been used [30, 37]. Interaction with the analyte can change the effective refractive index of the WGM, shifting its resonance frequency; this frequency (or wavelength) shift is often used for detection, of nanoparticles [27], of temperature [26], and for optomechanical chemical sensing [15]. Frequency splitting in coupled resonators can also be used, e.g., for biosensing [16]. In addition, absorption in the analyte can effectively increase the intrinsic loss, leading to a reduction in the measured Q of the WGM, and thus another sensing method. Absorption can also be detected via observation of the subsequent fluorescence [28].

In contrast to these methods, the absorption sensing technique used here makes use of the change in the relative depth of the WGM resonance dip [32–35]. The dip depth depends on the ratio of the two losses, and is maximum (100%) when the intrinsic and coupling losses are equal—critical coupling. If the WGM is undercoupled (intrinsic loss greater), an increase in intrinsic loss due to analyte absorption causes the dip to become shallower, whereas if the WGM is overcoupled (coupling loss greater) the dip will become deeper. Because it is the fractional depth that is measured by comparing throughput on resonance to throughput off resonance, the method is insensitive to laser power changes and insensitive to frequency drifts. As will be shown below, this technique of measuring change in dip depth [32] can be significantly more sensitive than measuring change in Q (i.e., change in WGM linewidth). This method is demonstrated here with preliminary results for the (internal) absorption sensing of methane (CH_4) in air and dye (SDA2072) in methanol solution.

3.2. Results

The trace gas detection method uses molecular vibrational overtone absorption lines in the 1580–1660 nm window. The narrow absorption lines of the CH_4 used here can affect WGM characteristics only in very specific frequency regions, of the order of a few GHz in width. The reference cell in figure 4 aids in finding these absorption lines. Not shown in figure 4 is the WGM strain-tuning apparatus that allows WGMs to be shifted into and out of CH_4 absorption lines by piezoelectric control of lengthwise stretching of the HBR.

Also not shown in figure 4 is the gas handling and pressure measurement system. Once the CH_4/air mixture is introduced into the system, CH_4 absorption lines around 1650 nm are identified by detecting the power transmitted through the 16.5 cm reference cell as the laser is frequency-scanned over a range of 18 GHz.

A preliminary result demonstrating the potential of HBRs for use as (internal) gas sensors is presented here. An experiment was performed using a silica HBR, similar to the one in figure 3 but with a central wall thickness smaller than 5 μm. The variation in the dip depth of the WGM in figure 6 shows that detection thresholds substantially lower than 0.1% (partial pressure) can easily be obtained with a thin-walled resonator around 1640 nm.

The fractional dip depth of the overcoupled sensing WGM in figure 6 increases from $M_i = 0.317$ at wavelengths longer than that of the main CH_4 absorption resonance (top trace) to $M = 0.503$ on resonance, a change of 59%. The dip depth depends on the ratio $x = \kappa^2/\alpha L$ of tapered-fiber coupling loss per round trip to other loss per round trip (L is the

microresonator circumference) as

$$M = \frac{4x}{(1+x)^2}. \tag{1}$$

A subscript i indicates that the other loss is intrinsic only —no loss due to analyte absorption. The measured dip depths here indicate that $x_i = 10.5$ and that it is reduced by the resonant gas absorption to $x = 5.78$. The Q of a WGM depends inversely on the total loss and can be written as

$$Q = \frac{2\pi nL}{\lambda\left(\kappa^2 + \alpha L\right)} = \frac{2\pi nL}{\lambda\kappa^2\left(1 + x^{-1}\right)}, \tag{2}$$

where n is the effective refractive index of the WGM (about 1.43 here) and λ is the wavelength. Note that this means that

$$\frac{Q}{Q_i} = \frac{1 + x_i^{-1}}{1 + x^{-1}} = 0.935, \tag{3}$$

indicating that the decrease in Q (or corresponding increase in WGM linewidth) is only 6.5%, in contrast to the 59% change in dip depth. This is in rough agreement with a measurement of mode widths (here $Q_i = 4.9 \times 10^6$), confirming that dip depth change is a more sensitive measure of analyte absorption [32]. Analyte absorption increases the loss coefficient from α_ι to

$$\alpha = \alpha_i + f\alpha_a, \tag{4}$$

where α_α is the analyte absorption coefficient and f is the (internal) evanescent fraction, the part of the mode volume interacting with the analyte. With this, the inverse loss ratio becomes

$$\frac{1}{x} = \frac{1}{x_i} + \frac{f\alpha_a L}{\kappa^2} = \frac{1}{x_i} + \frac{\lambda\left(1 + x_i^{-1}\right)}{2\pi n} Q_i f \alpha_a. \tag{5}$$

This expression shows that the sensitivity depends on the product $Q_i f$ of the WGM quality factor and the (internal, here) evanescent mode fraction. As discussed below, we do not know the mode indices and so cannot calculate *f a priori*, but the 1% CH_4/air absorption coefficient can be calculated from data in the literature [38, 39], particularly the HITRAN database. Doing so for the main absorption line, whose frequency is 6093.21 cm^{-1}, gives $\alpha_a = 1.48 \times 10^{-1}\ cm^{-1}$, and then equation (5) gives $f = 0.54\%$. This value is reasonable, being about three times as large as a typical external evanescent fraction [33].

Also note that as the WGM is shifted to shorter wavelengths, its dip depth decreases to only 0.385. The fact that this value is slightly greater than in the longer-wavelength off-resonance region is explained by the WGM's positioning between the two absorption features located at 6093.21 and 6093.49 cm^{-1}, as shown in figure 6. (They are thus separated by 8.4 GHz; the apparent 6 GHz separation in figure 6 appears to be the result of a scan range miscalibration.) Using pressure broadening data from the literature [38, 39], the linewidths in the 1% CH_4/air mixture are about 4 GHz, so they overlap a bit; in the bottom trace in figure 6, at a lower pressure in the reference cell with pure CH_4, Doppler broadening and pressure broadening contribute approximately equally to the linewidths of about 1 GHz.

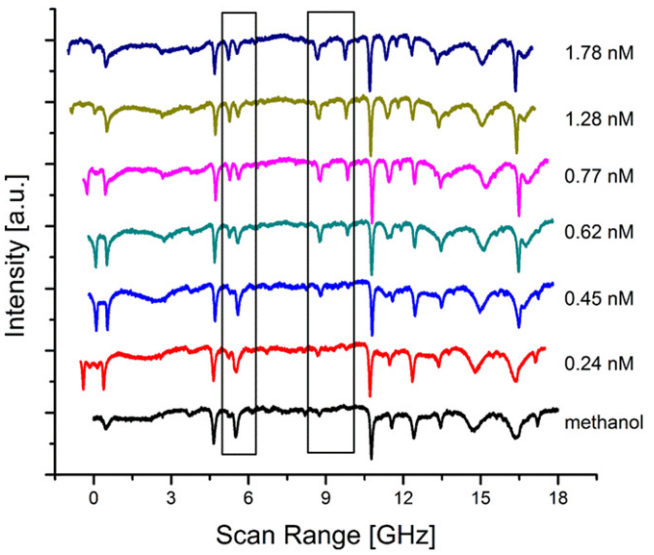

Figure 7. Set of WGMs at different analyte concentrations. The frequency-scan traces are displaced upward with increasing analyte concentration. Of the four highlighted WGMs (boxed), three are overcoupled (dip depth increases with concentration) and one is undercoupled.

A WGM in an HBR is described by three mode indices [14]: the azimuthal index m is the number of wavelengths in the circumference, the radial index p is the number of radial intensity maxima, and the axial index q is the number of axial field nodes. For the HBRs used here, $m \approx 2740$; the frequency spacing of modes of adjacent values of m (keeping the other mode indices constant) is about 67 GHz. The frequency spacings of modes of adjacent values of p and q are approximately 1295 GHz and 25 GHz, respectively. Because of the large values of m and the various free spectral ranges, we cannot reliably assign mode indices because of the uncertainty of our HBR radius measurement and the limited (18 GHz) scan range. From the observed spectral density of modes (a little less than 1 per GHz), we can estimate that WGMs with q values ranging from 0 to 7 and p values ranging from 1 to 6 are excited in figures 6 and 7. Calculations of the radial mode profiles indicate that WGMs with $p > 1$ should have internal evanescent fractions in the results shown in figure 6 (thinner wall, air inside) and in figure 7 (thicker wall, methanol inside).

A preliminary qualitative result featuring liquid sensing, specifically the NIR-active dye SDA2072, is shown in figure 7. In this experiment, small volumes of methanol-diluted SDA2072 were introduced into a silica HBR similar to the one in figure 3, with a wall thickness of about 10 μm and WGMs excited by a laser at 1581 nm. The variation of the dip depth for the boxed WGMs, which have Q values ranging from (1–3) $\times 10^6$, is a clear indicator that these microresonators' internal evanescent fractions of higher-radial-order WGMs are responsible for sensing of the broadband absorption in the dye. Specifically, in the experimental results

outlined in figure 7, the boxed WGMs show strong detection sensitivity for sub-nanomolar levels of SDA2072, even though the absorption coefficient of the solvent, methanol, is five orders of magnitude larger than that of SDA2072 at this wavelength [32, 35].

4. Conclusions and future work

A simple and cost-effective three-step method for fabricating silica HBRs for optical sensing was outlined. The procedure used commercial off the shelf capillaries of different external diameters (320 and 800 μm). The steps include the HF-mediated automated etching procedure, the removal of the capillary's polyimide coating, and the use of a H_2/O_2 jeweler's torch in conjunction with a so-called 'soften and pressurize' procedure. Following these steps, HBRs with wall thicknesses between 5 and 10 μm could be obtained. The bottle shape and the smooth interior surface enable Q values as high as 10^8 to be obtained.

Additionally, it was shown that these thin walled HBRs can be used as internal evanescent wave WGM-based optical absorption sensing devices for NIR-active gases. The detection threshold for a mixture of CH_4 in air was determined to be substantially less than 0.1% (partial pressure). The detection threshold could easily be lowered by an order of magnitude with the help of WGM locking and lock-in detection techniques [33]. Although this detection threshold was modest, this preliminary result indicated that internal sensing for NIR-active gases can be easily accomplished using silica HBRs. A three-order-of-magnitude improvement in detection threshold (to well below the ppm level) could be accomplished by exciting fundamental vibrational modes rather than overtones. This could be done using HBRs produced from fluoride glasses and exciting the WGMs in these HBRs with frequency scanned interband cascade or quantum cascade lasers that emit at wavelengths longer than 3.5 μm.

For sensing of liquid chemical solutions, sensitivities better than those for immersed microspheres [35] were demonstrated. Furthermore, internal sensing has the advantage of requiring much less analyte.

Finally, the internal evanescent field of a silica HBR can, of course, also be used in frequency-shift sensing experiments [15, 16, 26, 27, 30, 37]. An advantage of the HBR is that its sensitivity to other frequency shifts, such as those due to temperature changes, can be greatly reduced. This is because some WGMs have no internal evanescent fields (see figure 5), and so will undergo no analyte-dependent frequency shifts, allowing them to be used as references for the relative frequency shifts of those WGMs that are sensitive to the analyte. Results of experiments using such relative frequency shifts to sense changes in pH will be reported elsewhere; these experiments employ swellable polymers coating the interior surface of an HBR [40].

Acknowledgments

The authors thank Mike Lucas and the staff of the Oklahoma State University Physics and Chemistry Instrument Shop for their assistance in construction of mechanical parts for the syringe pump used in this work.

References

[1] White I M, Oveys H and Fan X 2006 Liquid-core optical ring-resonator sensors *Opt. Lett.* **31** 1319–21
[2] Zhu H, White I M, Suter J D, Zourob M and Fan X 2007 Integrated refractive index optical ring resonator detector for capillary electrophoresis *Anal. Chem.* **79** 930–7
[3] Shopova S I, White I M, Sun Y, Zhu H, Fan X, Frye-Mason G, Thompson A and Ja S 2008 On-column micro gas chromatography detection with capillary-based optical ring resonators *Anal. Chem.* **80** 2232–6
[4] Sun Y, Shopova S I, Frye-Mason G and Fan X 2008 Rapid chemical-vapor sensing using optofluidic ring resonators *Opt. Lett.* **33** 788–90
[5] Sun Y, Shopova S I, White I M, Frye-Mason G and Fan X 2009 Rapid chemical vapor detection using optofluidic ring resonators *Advanced Photonic Structures for Biological and Chemical Detection* ed X Fan (Berlin: Springer) pp 123–43
[6] White I M, Zhu H, Suter J D and Fan X 2009 Label-free biosensing with the optofluidic ring resonator *Advanced Photonic Structures for Biological and Chemical Detection* ed X Fan (Berlin: Springer) pp 377–93
[7] Sumetsky M 2004 Whispering-gallery-bottle microcavities: the three-dimensional etalon *Opt. Lett.* **29** 8–10
[8] Louyer Y, Meschede D and Rauschenbeutel A 2005 Tunable whispering-gallery-mode resonators for cavity electrodynamics *Phys. Rev.* A **72** 031801 (R)
[9] Pöllinger M, O'Shea D, Warken F and Rauschenbeutel A 2009 Ultrahigh-Q tunable whispering-gallery-mode microresonator *Phys. Rev. Lett.* **103** 053901
[10] Murugan G S, Wilkinson J S and Zervas M N 2009 Selective excitation of whispering gallery modes in a novel bottle microresonator *Opt. Express* **17** 11916–25
[11] O'Shea D, Junge C, Nickel S, Pöllinger M and Rauschenbeutel A 2011 Ultra-high Q whispering-gallery-mode bottle microresonators: properties and applications *Proc. SPIE* **7913** 79130N
[12] O'Shea D, Junge C, Volz J and Rauschenbeutel A 2013 Fiber-optical switch controlled by a single atom *Phys. Rev. Lett.* **111** 193601
[13] Strelow C, Rehberg H, Schultz C M, Welsch H, Heyn C, Heitmann D and Kipp T 2008 Optical microcavities formed by semiconductor microtubes using a bottlelike geometry *Phys. Rev. Lett.* **101** 127403
[14] Murugan G S, Petrovich M N, Jung Y, Wilkinson J S and Zervas M N 2011 Hollow-bottle optical microresonators *Opt. Express* **19** 20773–84
[15] Bahl G, Kim K H, Lee W, Liu J, Fan X and Carmon T 2013 Brillouin cavity optomechanics with microfluidic devices *Nat. Commun.* **4** 1994
[16] Li M, Wu X, Liu L, Fan X and Xu L 2013 Self-referencing optofluidic ring resonator sensor for highly sensitive biomolecular detection *Anal. Chem.* **85** 9328–32
[17] Li H, Guo Y, Sun Y, Reddy K and Fan X 2010 Analysis of single nanoparticle detection by using 3-dimensionally confined optifluidic ring resonators *Opt. Express* **18** 25081–8

[18] Berneschi S, Farnesi D, Cosi F, Nunzi Conti G, Pelli S, Righini G C and Soria S 2011 High *Q* silica microbubble resonators fabricated by arc discharge *Opt. Lett.* **36** 3521–3
[19] Farnesi D, Brucci A, Berneschi S, Brenci M, Cosi F, Nunzi Conti G, Pelli S, Righini G C and Soria S 2012 High *Q* silica microbubble resonators *Proc. SPIE* **8264** 826417
[20] Sumetsky M, Dulashko Y and Windeler R S 2010 Optical microbubble resonator *Opt. Lett.* **35** 898–900
[21] Sumetsky M, Dulashko Y and Windeler R S 2010 Super free spectral range tunable optical microbubble resonator *Opt. Lett.* **35** 1866–8
[22] Watkins A, Ward J, Wu Y and Nic Chormaic S 2011 Single-input spherical microbubble resonator *Opt. Lett.* **36** 2113–5
[23] Lee W, Sun Y, Li H, Reddy K, Sumetsky M and Fan X 2011 A quasi-droplet optofluidic ring resonator laser using a micro-bubble *Appl. Phys. Lett.* **99** 091102
[24] Henze R, Seifert T, Ward J and Benson O 2011 Tuning whispering gallery modes using internal aerostatic pressure *Opt. Lett.* **36** 4536–8
[25] Li M, Wu X, Liu L and Xu L 2013 Kerr parametric oscillations and frequency comb generation from dispersion compensated silica micro-bubble resonators *Opt. Express* **21** 16908–13
[26] Ward J M, Yang Y and Nic Chormaic S 2013 Highly sensitive temperature measurements with liquid-core microbubble resonators *IEEE Photonics Technol. Lett.* **25** 2350–3
[27] Yang Y, Ward J and Nic Chormaic S 2014 Quasi-droplet microbubbles for high resolution sensing applications *Opt. Express* **22** 6881–98
[28] Cohoon G A, Kieu K and Norwood R A 2014 Observation of two-photon fluorescence for Rhodamine 6G in microbubble resonators *Opt. Lett.* **39** 3098–101
[29] Wang P, Ward J, Yang Y, Feng X, Brambilla G, Farrell G and Nic Chormaic S 2015 Lead-silicate glass optical microbubble resonator *Appl. Phys. Lett.* **106** 061101
[30] Ward J M, Dhasmana N and Nic Chormaic S 2014 Hollow core, whispering gallery resonator sensors *Eur. Phys. J. Spec. Top.* **223** 1917–35
[31] Cosci A, Quercioli F, Farnesi D, Berneschi S, Giannetti A, Cosi F, Barucci A, Nunzi Conti G, Righini G and Pelli S 2015 Confocal reflectance microscopy for determination of microbubble resonator thickness *Opt. Express* **23** 16693–701
[32] Rosenberger A T 2007 Analysis of whispering-gallery microcavity-enhanced chemical absorption sensors *Opt. Express* **15** 12959–64
[33] Farca G, Shopova S I and Rosenberger A T 2007 Cavity-enhanced laser absorption spectroscopy using microresonator whispering-gallery modes *Opt. Express* **15** 17443–8
[34] Rosenberger A T and Rezac J P 2001 Whispering-gallery-mode evanescent-wave microsensor for trace-gas detection *Proc. SPIE* **4265** 102–12
[35] Farca G, Shopova S I and Rosenberger A T 2005 Intracavity chemical absorption sensing using microresonator whispering-gallery modes *Proc. SPIE* **5855** 427–30
[36] Lee Y-I, Park K-H, Lee J, Lee C-S, Kim H J C-J and Yoon Y-S 1997 Dry release for surface micromachining with HF vapor-phase etching *J. Microelectromech. Syst.* **6** 226–33
[37] Foreman M R, Swaim J D and Vollmer F 2015 Whispering gallery mode sensors *Adv. Opt. Photonics* **7** 168–240
[38] Margolis J S 1988 Measured line positions and strengths of methane between 5500 and 6180 cm^{-1} *Appl. Opt.* **27** 4038–51
[39] Rothman L S *et al* 2013 The HITRAN2012 molecular spectroscopic database *J. Quant. Spectrosc. Radiat. Transfer* **130** 4–50
[40] Stoian R I, Lavine B K and Rosenberger A T 2015 pH sensing using whispering gallery modes of a silica hollow bottle resonator *Preprint*